



# Effect of Hydrogen Gas Pressure on Calcium–Aluminum-rich Inclusion Formation in the Protosolar Disk: a Laboratory Simulation of Open-system Melt Crystallization

Michiru Kamibayashi<sup>1</sup>, Shogo Tachibana<sup>1,2</sup>, Daiki Yamamoto<sup>2</sup>, Noriyuki Kawasaki<sup>3</sup>, and Hisayoshi Yurimoto<sup>3</sup><sup>1</sup>Department of Earth and Planetary Science, The University of Tokyo, Hongo, Tokyo, 113-0033, Japan; [michiru@eps.s.u-tokyo.ac.jp](mailto:michiru@eps.s.u-tokyo.ac.jp)<sup>2</sup>Institute of Space and Astronautical Science, Japan Aerospace Exploration Agency, Sagamihara, Kanagawa, 252-210, Japan<sup>3</sup>Department of Natural History Sciences, Hokkaido University, Sapporo, Hokkaido 060-0810, Japan

Received 2021 October 18; revised 2021 November 9; accepted 2021 November 22; published 2021 December 10

## Abstract

Calcium–aluminum-rich inclusions (CAIs) are the oldest materials that formed in the protosolar disk. Igneous CAIs experienced melting and subsequent crystallization in the disk during which the evaporation of relatively volatile elements such as Mg and Si occurred. Evaporation from the melt would have played a significant role in the variation of chemical, mineralogical, and petrologic characteristics of the igneous CAIs. In this study, we investigated crystallization of CAI analog melt under disk-like low-pressure hydrogen ( $P_{\text{H}_2}$ ) conditions of 0.1, 1, and 10 Pa to constrain the pressure condition of the early solar system in which type B CAIs were formed. At  $P_{\text{H}_2} = 10$  Pa, the samples were mantled by melilite crystals, as observed for type B1 CAIs. However, the samples heated at  $P_{\text{H}_2} = 0.1$  Pa exhibited random distribution of melilite, as in type B2 CAIs. At the intermediate  $P_{\text{H}_2}$  of 1 Pa, type-B1-like structure formed when the cooling rate was  $5^\circ\text{C hr}^{-1}$ , whereas the formation of type-B2-like structure required a cooling rate faster than  $20^\circ\text{C hr}^{-1}$ . The compositional characteristics of melilite in type B1 and B2 CAIs could also be reproduced by experiments. The results of the present study suggest that  $P_{\text{H}_2}$  required for type-B1-like textural and chemical characteristics is greater than 1 Pa. The hydrogen pressure estimated in this study would impose an important constraint on the physical condition of the protosolar disk where type B CAIs were formed.

*Unified Astronomy Thesaurus concepts:* Meteorites (1038); Cosmochemistry (331); Chondrites (228); Protoplanetary disks (1300); Astrochemistry (75); Solar system formation (1530)

## 1. Introduction

Calcium–aluminum-rich inclusions (CAIs), found in undifferentiated meteorites (chondrites), are the oldest materials formed in the solar system ( $4567.30 \pm 0.16$  Ma; Amelin et al. 2010; Connelly et al. 2012). They consist of refractory minerals that are predicted to be the first phases to condense out of a cooling gas of solar composition (e.g., Grossman 1972, 2010). The presence of CAIs requires high-temperature processes in the very early stage of solar system formation, but the details of the CAI-forming environment have not yet been clarified.

Type B CAIs are millimeter-to-centimeter-sized coarse-grained inclusions consisting mainly of spinel, melilite, fassaite, and anorthite. They are texturally subdivided into type B1s and type B2s (e.g., Wark & Lovering 1982). Type B1 CAIs have a continuous outer layer of melilite ( $\text{Ca}_2\text{Al}_2\text{SiO}_7$  (gehlenite)– $\text{Ca}_2\text{MgSi}_2\text{O}_7$  (åkermanite)) enclosing the interior part consisting of randomly distributed spinel, melilite, fassaite, and anorthite. Such mantle melilite is absent from type B2 CAIs. Petrological studies and experimental investigations of coarse-grained type B CAIs have concluded that both type B1 and B2 CAIs have gone through the molten stage at a maximum temperature of  $\sim 1400^\circ\text{C}$  and are the products of crystallization from a liquid cooled at rates of  $0.1\text{--}50^\circ\text{C hr}^{-1}$  (MacPherson & Grossman 1981; Stolper 1982; Stolper & Paque 1986; Yamamoto et al. 2021).

Type B CAIs are enriched in heavy isotopes of relatively volatile elements such as Mg and Si (Clayton et al. 1988), most

likely due to the evaporation of Mg and Si from the melt (e.g., Davis et al. 1990; Grossman et al. 2000; Richter et al. 2002, 2007; Mendybaev et al. 2021). It is known that the evaporation rates of minerals increase with increasing partial pressure of hydrogen ( $\text{H}_2$ ), which is the most abundant gas in protoplanetary disks (e.g., Nagahara & Ozawa 1996; Tachibana & Tsuchiyama 1998; Tsuchiyama et al. 1998; Tachibana et al. 2002; Takigawa et al. 2009) and evaporation experiments on CAI analog melts have confirmed that the evaporation of Mg and Si from CAI melts is also promoted in the presence of hydrogen gas (Richter et al. 2002; Shahar & Young 2007; Mendybaev et al. 2021).

The evaporation of Mg and Si during the melting and crystallization of type B CAIs depends on the hydrogen pressure, whereas elemental diffusion within the melt does not. Mendybaev et al. (2006) conducted experiments on the crystallization of CAI analog melt at 1 atm of hydrogen-dominant gas and showed that the melilite mantle in type B1 CAIs can form under reducing conditions. They concluded that the evaporation of Mg and Si dominates their diffusion within the melt under reducing conditions and the melt at the outer part of the droplet is enriched with Ca and Al compared to Mg and Si, leading to the preferential crystallization of melilite at the melt surface. However, it is necessary to conduct experiments under actual low-pressure hydrogen conditions of the early solar system.

Here, we investigated the effect of evaporation during the crystallization of type B CAIs on their chemical and textural characteristics through laboratory experiments in a protoplanetary disk-like low-pressure hydrogen gas atmosphere. The results are discussed to impose a constraint on the hydrogen

pressure of the protosolar disk during type B CAI formation, which is an important but less constrained disk parameter.

## 2. Experimental Methods

### 2.1. Preparation of Starting Material

The chemical composition of the starting material used in the experiments was similar to composition  $\chi$  falls on the trajectory of equilibrium condensation from a gas of solar composition at the total pressure of 1 Pa (Grossman et al. 2002; hereafter referred to as CAI $\chi$ ). The evaporation of Mg and Si from CAI $\chi$  results in a composition that falls in the field of the bulk composition of most type B CAIs (Grossman et al. 2002). The starting material was prepared by mixing SiO<sub>2</sub>, TiO<sub>2</sub>, Al<sub>2</sub>O<sub>3</sub>, MgO, and CaCO<sub>3</sub> reagent powders with 25.71 wt% SiO<sub>2</sub>, 1.11 wt% TiO<sub>2</sub>, 33.23 wt% Al<sub>2</sub>O<sub>3</sub>, 13.64 wt% MgO, and 26.30 wt% CaO. These powders were ground under ethanol in an alumina mortar for  $\sim$ 1 hr, dried at room temperature, and slowly heated to 1000°C for 10 hr in a muffle furnace in a platinum crucible to remove CO<sub>2</sub> from CaCO<sub>3</sub>. The platinum crucible was then heated in a Keramax vertical tube furnace (Nikkato Corporation TS-4B06) to 1525°C for 24 hr and quenched in air. The resulting glass + spinel assemblage was ground into a powder in an alumina mortar and used as the starting material.

### 2.2. Crystallization Experiments

Samples for experiments under low-pressure hydrogen were prepared by fixing a mixture of 20–40 mg of the starting material and polyvinyl alcohol as a binder onto a 2.5 mm diameter iridium wire loop (Mendybaev et al. 2021). The samples were premelted by heating in air at 1520°C for 2 hr using the Keramax furnace or in vacuum ( $< \sim 10^{-1}$  Pa) at 1600°C for 10 minutes and then at 1450°C for 10 hr using a vacuum furnace, as described below. The premelted samples were spherical and 2–3 mm in size, which is within the size range of type B CAIs (MacPherson & Grossman 1981; Podosek et al. 1991; Simon & Grossman 2006; Bullock et al. 2013).

Crystallization experiments under low-pressure hydrogen conditions were conducted at  $P_{\text{H}_2}$  of 0.1, 1, and 10 Pa with a maximum temperature of 1420°C in a high-temperature vacuum furnace (Takigawa et al. 2009; Mendybaev et al. 2021) (Table 1). The maximum temperature of 1420°C was  $\sim 20^\circ\text{C}$  higher than the liquidus temperature of melilite ( $1402.5 \pm 2.5^\circ\text{C}$ ) for the CAI $\chi$  composition, which was determined by a series of isothermal crystallization experiments in air (Table 1). Experimental details of isothermal crystallization experiments in air are the same as those described by Yamamoto et al. (2021).

The heating temperature was monitored and controlled with a type C (W<sub>95</sub>Re<sub>5</sub>–W<sub>74</sub>Re<sub>26</sub>) thermocouple placed 22.5 mm above the sample location. The thermocouple was pre-calibrated against the melting point of Au (1064.4°C) and Ni (1455°C) by placing the respective metals at the sample location. The pressure inside the furnace was measured using a Pirani vacuum gauge and an ionization vacuum gauge (ULVAC M-13). A proper pressure conversion factor for H<sub>2</sub> was used (the actual hydrogen pressure was converted as twice the indicated pressure) when hydrogen gas was introduced into the furnace.

The premelted sample was hung on the sample holder, and the vacuum chamber was evacuated until the pressure

decreased to below  $5 \times 10^{-4}$  Pa. The sample was then preheated at 500°C for  $\sim$ 1 hr to evacuate the absorbed gas in the vacuum chamber. Once the pressure decreased below  $5 \times 10^{-4}$  Pa, the sample was heated to 1420°C at a rate of  $\sim 20^\circ\text{C minute}^{-1}$ . As soon as the temperature gets to 1420°C, hydrogen gas (99.99%) was introduced into the furnace from a hydrogen gas cylinder through alumina tubes and exhausted from the bottom of the vacuum chamber by the pumping system. The hydrogen flow rate was adjusted using a variable leak valve or mass flow controllers (Kofloc 3660) to maintain  $P_{\text{H}_2}$  with a fluctuation of  $< 20\%$ . After heating for 1 hr at 1420°C, the sample was cooled at a controlled cooling rate of 5, 20, or 50°C hr<sup>-1</sup> and quenched at 1100–1300°C by turning off the heater (the temperature dropped down to the sample solidus temperature of approximately 1000°C at the rate of  $\sim 500^\circ\text{C minute}^{-1}$ ). Isothermal experiments at 1420°C and  $P_{\text{H}_2}$  of 1 and 10 Pa were also performed for comparison. In the isothermal experiments, the samples were quenched from 1420°C after the desired heating duration by turning off the heater.

### 2.3. Analytical Procedure

The sample weights were measured before and after the experiments using an electric ultra-microbalance (Mettler Toledo XP2U) with a precision of  $\pm 0.1 \mu\text{g}$  to estimate the amount of evaporation from the melt. The weight loss was attributed to sample evaporation because evaporation of the iridium wire was negligibly small ( $< 0.2\%$  of the initial mass) based on a blank experiment.

The starting material and run products were mounted into epoxy and polished down to a roughness of 0.5–1  $\mu\text{m}$  along the orthogonal plane to the wire loop. Textural observations and quantitative elemental analyses were conducted using scanning electron microscopes (JEOL JSM-7000F; Hitachi SU-6600) equipped with an energy dispersive X-ray spectrometer (Oxford X-Max150) operated at an acceleration voltage of 15 kV. Details of the elemental analysis by JEOL JSM-7000F is described in Kawasaki et al. (2018, 2019). The built-in standardization database at 15 kV in the Oxford AZtec software was used for the elemental analysis with Hitachi SU-6600. Quantitative elemental maps of Mg, Si, and Al were converted to quantitative compositional maps of melilite using the ImageJ software.

## 3. Results

The samples after the crystallization experiments contained spinel, melilite,  $\pm$  pyroxene, and  $\pm$  anorthite (Figure 1, Table 1). The presence/absence of pyroxene and anorthite, which crystallize at  $< 1260^\circ\text{C}$  (Stolper 1982) for CAIB melt, depends mainly on the quenching temperatures of the run products, and does not affect discussion of the crystallization of melilite in this study.

The textural and compositional characteristics of melilite varied with  $P_{\text{H}_2}$  and cooling rate. At  $P_{\text{H}_2} = 0.1$  Pa, all the samples showed randomly distributed melilite crystals similar to type B2 CAIs (Figure 1(a)), while at  $P_{\text{H}_2} = 10$  Pa, the outermost part of all the samples was mantled by melilite crystals like type B1 CAIs (Figure 1(c)). At  $P_{\text{H}_2} = 1$  Pa, the sample cooled at  $5^\circ\text{C hr}^{-1}$  had a continuous melilite mantle as at  $P_{\text{H}_2} = 10$  Pa; in contrast, incomplete melilite mantle was

**Table 1**  
Experimental Conditions and Results of Isothermal and Dynamic Crystallization Experiments in Air and Low-pressure Hydrogen

Run	$T_{\max}$ (°C)	$T_{\text{quench}}$ (°C)	Duration at $T_{\max}$ (hr)	Gas Comp. (Pressure in Pa)	Cooling Rate (°C hr <sup>-1</sup> )	Wt. Loss		Major Phases <sup>a</sup>	Melilite Comp. (Åk%)	Texture <sup>b</sup>
						(%)	(mg cm <sup>-2</sup> )			
<i>Isothermal experiments in air</i>										
97	1420	1420	12	air	/	/	/	gl + sp	/	/
106	1410	1410	12	air	/	/	/	gl + sp	/	/
351	1405	1405	12	air	/	/	/	gl + sp + mel	21 ± 2 <sup>c</sup>	/
104	1400	1400	12	air	/	/	/	gl + sp + mel	22 ± 2 <sup>c</sup>	/
81	1380	1380	12	air	/	/	/	gl + sp + mel	26 ± 2 <sup>c</sup>	/
94	1360	1360	12	air	/	/	/	gl + sp + mel	32 ± 2 <sup>c</sup>	/
<i>Dynamic crystallization experiments in low-pressure hydrogen</i>										
191	1420	1120	1	H <sub>2</sub> (0.1)	50	2.1	2.9	gl + sp + mel + px	31–72 <sup>d</sup>	B2-like
UT-16	1420	1120	1	H <sub>2</sub> (0.1)	50	0.7	0.83	gl + sp + mel + px	38–63 <sup>d</sup>	B2-like
198	1420	1120	1	H <sub>2</sub> (0.1)	20	4.9	6.5	gl + sp + mel + px	27–66 <sup>d</sup>	B2-like
UT-18	1420	1120	1	H <sub>2</sub> (0.1)	20	3.0	3.7	gl + sp + mel + px	38–72 <sup>d</sup>	B2-like
274	1420	1120	1	H <sub>2</sub> (0.1)	5	10.7	14.6	gl + sp + mel + px	18–32 <sup>d</sup>	B2-like
329	1420	1120	1	H <sub>2</sub> (1)	50	5.2	5.5	gl + sp + mel + px	19–52 <sup>d</sup>	partially mantled
UT-14	1420	1120	1	H <sub>2</sub> (1)	50	3.8	4.4	gl + sp + mel + px	21–57 <sup>d</sup>	partially mantled
332	1420	1120	1	H <sub>2</sub> (1)	20	8.8	9.7	gl + sp + mel + px	16–54 <sup>d</sup>	partially mantled
UT-3	1420	1100	1	H <sub>2</sub> (1)	5	17.1	20.2	gl + sp + mel + px + an	7–62 <sup>d</sup>	B1-like
UT-37	1420	1100	1	H <sub>2</sub> (1)	5	9.9	12.0	gl + sp + mel + px + an	9–38 <sup>d</sup>	B1-like
353	1420	1120	1	H <sub>2</sub> (10)	50	6.8	8.2	gl + sp + mel + px	12–58 <sup>d</sup>	B1-like
UT-21	1420	1120	1	H <sub>2</sub> (10)	50	10.0	11.9	gl + sp + mel + px	10–52 <sup>d</sup>	B1-like
UT-30	1420	1100	1	H <sub>2</sub> (10)	20	7.8	9.5	gl + sp + mel + px + an	13–60 <sup>d</sup>	B1-like
356	1420	1235	1	H <sub>2</sub> (10)	5	14.1	15.8	gl + sp + mel	11–21 <sup>d</sup>	B1-like
UT-23	1420	1100	1	H <sub>2</sub> (10)	5	10.4	13.8	gl + sp + mel + px + an	9–65 <sup>d</sup>	B1-like
UT-27	1420	1300	1	H <sub>2</sub> (10)	5	12.5	14.6	gl + sp + mel	10–19 <sup>d</sup>	B1-like
<i>Isothermal experiments in low-pressure hydrogen</i>										
UT-12	1420	/	1	H <sub>2</sub> (1)	/	3	/	gl + sp + mel	33–39 <sup>d</sup>	dendritic
UT-43	1420	/	5	H <sub>2</sub> (1)	/	11	/	gl + sp + mel	8–31 <sup>d</sup>	B1-like/dendritic
UT-35	1420	/	15	H <sub>2</sub> (1)	/	10	/	gl + sp + mel	7–34 <sup>d</sup>	B1-like/dendritic
UT-41	1420	/	45	H <sub>2</sub> (1)	/	20	/	gl + sp + mel	7–24 <sup>d</sup>	B1-like/dendritic
UT-33	1420	/	1	H <sub>2</sub> (10)	/	6	/	gl + sp + mel	12–32 <sup>d</sup>	B1-like/dendritic

#### Notes.

<sup>a</sup> Abbreviations: gl = glass; sp = spinel; mel = melilite; px = pyroxene; an = anorthite.

<sup>b</sup> B2-like: randomly distributed melilite crystals in the sample. B1-like: the sample surface is continuously surrounded by melilite crystals, similar to type B1 CAIs.

<sup>c</sup> Average melilite composition obtained from the central parts of the grains. Errors are 1 SD of the mean.

<sup>d</sup> Melilite compositional ranges randomly obtained in the melilite crystals.

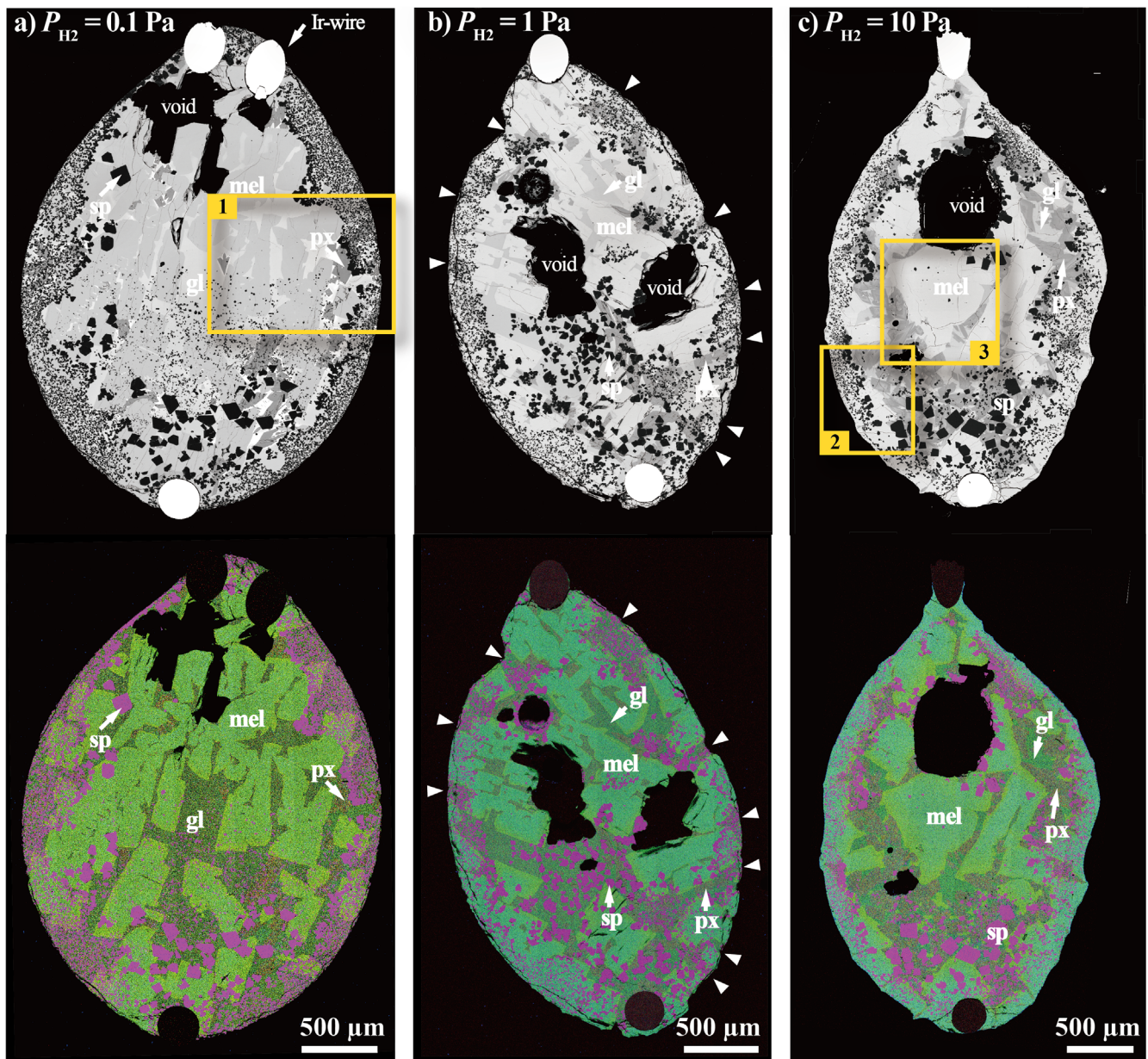
observed in the sample cooled at the rates of 20 and 50°C hr<sup>-1</sup> (Figure 1(b)).

In the sample cooled at 50°C hr<sup>-1</sup> and  $P_{\text{H}_2} = 0.1$  Pa (UT-14) (Figure 2(a)), the åkermanite (Åk) content (åkermanite molar concentration) increased from the core to the rim of the individual melilite grains. On the other hand, in the sample cooled at 50°C hr<sup>-1</sup> and  $P_{\text{H}_2} = 10$  Pa (353), melilite grains at the outer margin of the sample had the lowest åkermanite content (Åk<sub>~10–15</sub>) and became Åk-rich toward the interior (Figure 2(b)). Such Åk-poor melilite was observed only at the surface of the samples with melilite mantle. The melilite grains in the inner part (Figure 2(c)) showed the core-to-rim normal zoning similar to melilite in the samples heated at  $P_{\text{H}_2} = 0.1$  Pa (Figure 2(a)).

Histograms of melilite compositions in samples cooled at 5 and 50°C hr<sup>-1</sup> at different hydrogen pressures also show differences in melilite compositions (Figure 3; Table 1). At  $P_{\text{H}_2} = 0.1$  Pa, more Åk-poor melilite crystallized at the cooling rate of 5°C hr<sup>-1</sup> (Åk<sub>16–34</sub>; Figure 3(b)) than that at the cooling rate of 50°C hr<sup>-1</sup> (Åk<sub>31–72</sub>; Figure 3(a)). Such a decrease in the åkermanite content with slower cooling rate was also observed

at  $P_{\text{H}_2} = 1$  Pa (Figures 3(c), (d)). In contrast, at  $P_{\text{H}_2} = 10$  Pa, the samples exhibited a similar compositional range independent of the cooling rates (Figures 3(e), (f)). Samples with melilite mantle (5 and 50°C hr<sup>-1</sup> at  $P_{\text{H}_2} = 10$  Pa, and 5°C hr<sup>-1</sup> at  $P_{\text{H}_2} = 1$  Pa; Figures 3(d)–(f)) had melilite with the åkermanite contents considerably lower than Åk<sub>20</sub> (Åk<sub>~10</sub>), as seen in Figure 2(b).

The degree of weight loss of the samples, normalized to the sample surface area, is shown in Figure 4. Assuming the sample shape to be spherical for simplicity, the surface area was calculated from the initial mass of each sample and the melt density at 1420°C (2.77 g cm<sup>-3</sup>) calculated based on Lange & Carmichael (1987). These weight losses can be attributed to the evaporation of Mg and Si from the melt, as discussed in previous experiments in hydrogen gas (Richter et al. 2002; Mendybaev et al. 2021). At  $P_{\text{H}_2} = 0.1$  Pa, where no melilite mantle was formed at the sample surface irrespective of the cooling rate, weight losses increased with decreasing cooling rate. For instance, the weight loss of the sample cooled at 5°C hr<sup>-1</sup> was approximately one order of magnitude larger than that of the samples cooled at 50°C hr<sup>-1</sup>, which can be



**Figure 1.** Backscattered electron (BSE) images and combined X-ray elemental maps with Mg (red), Ca (green), and Al (blue) in samples heated at 1420°C for 1 hr and subsequently cooled at a cooling rate of 50°C hr<sup>-1</sup> at different hydrogen pressures. (a)  $P_{\text{H}_2} = 0.1$  Pa (UT-16; Table 1). The sample shows random distribution of melilite. (b)  $P_{\text{H}_2} = 1$  Pa (UT-14; Table 1). The sample surface is partially covered with melilite mantle. Triangles in (b) indicate regions where no melilite crystals were present at the sample surface. (c)  $P_{\text{H}_2} = 10$  Pa (353; Table 1). The sample exhibits well-developed melilite mantle. Detailed BSE images and quantitative maps of melilite in the areas indicated by yellow boxes are shown in Figure 2. gl = glass; sp = spinel; mel = melilite; px = pyroxene.

explained by the difference in the cooling timescale (Figure 4). At  $P_{\text{H}_2} = 10$  Pa, where the melilite rim was recognized in all the samples, we observed less difference in the weight losses associated with the cooling timescale (Figure 4). At a cooling rate of 50°C hr<sup>-1</sup>, the amount of evaporation was roughly proportional to the square root of  $P_{\text{H}_2}$  (i.e., the weight losses of the samples increase roughly by a factor of three with an increase in  $P_{\text{H}_2}$  by one order of magnitude), which is consistent with thermodynamically predicted  $P_{\text{H}_2}$  dependence of evaporation rates (Richter et al. 2002; Mendybaev et al. 2006). In contrast, at the slowest cooling rate of 5°C hr<sup>-1</sup>, the variation in weight losses of the samples was less than that expected from the  $P_{\text{H}_2}$  dependence of evaporation rates (Figure 4).

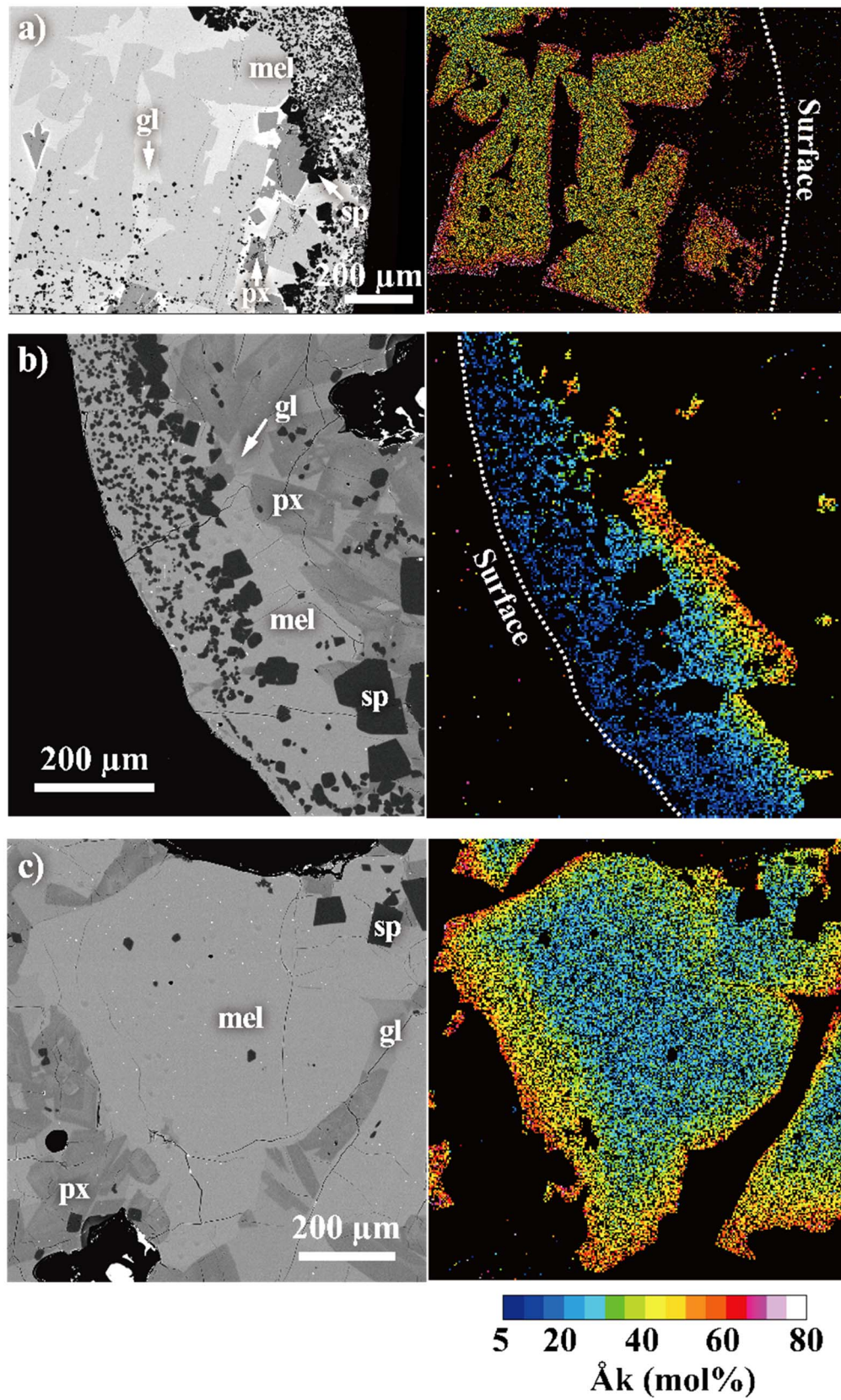
Isothermal heating experiments at a temperature 20°C above the melilite liquidus for the melt with CAI $\chi$  composition

showed that the sample heated at  $P_{\text{H}_2} = 1$  Pa for 1 hr exhibited only dendritic melilite with a composition of  $\text{Åk}_{\sim 33-39}$  (Table 1), which is expected to form during quenching. However, the samples heated for 5–45 hr exhibited preferential crystallization of coarse-grained melilite with low  $\text{Åk}_{\sim 7}$  at their surfaces (Table 1). Similar melilite at the sample surface was observed in the samples heated at 1420°C and  $P_{\text{H}_2} = 10$  Pa for 1 hr (Table 1).

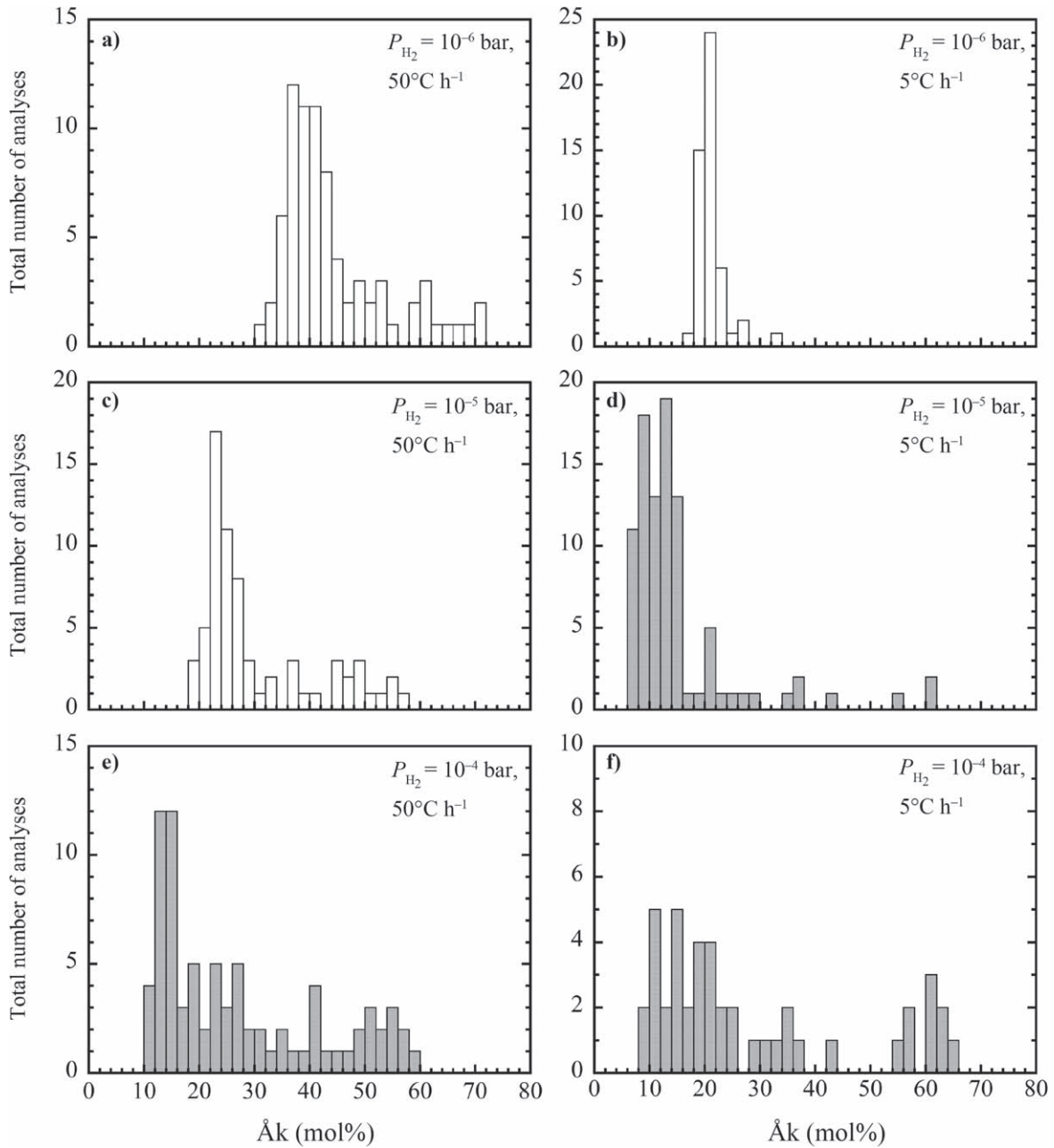
## 4. Discussion

### 4.1. Mechanism of Melilite Mantle Formation

We observed preferential crystallization of Al-rich melilite near the surface of the samples at  $P_{\text{H}_2} = 10$  Pa at all cooling



**Figure 2.** BSE images and quantitative maps of melilite in the areas shown in Figure 1. The compositional map shows the differences in åkermanite content ( $\text{\AA k}$ ). (a) Melilite in area 1 shown in Figure 1(a). (b) Melilite locates at the rim in area 2 shown in Figure 1(c). (c) Melilite located in the interior of the sample shown as area 3 in Figure 1(c). gl = glass; sp = spinel; mel = melilite; px = pyroxene.

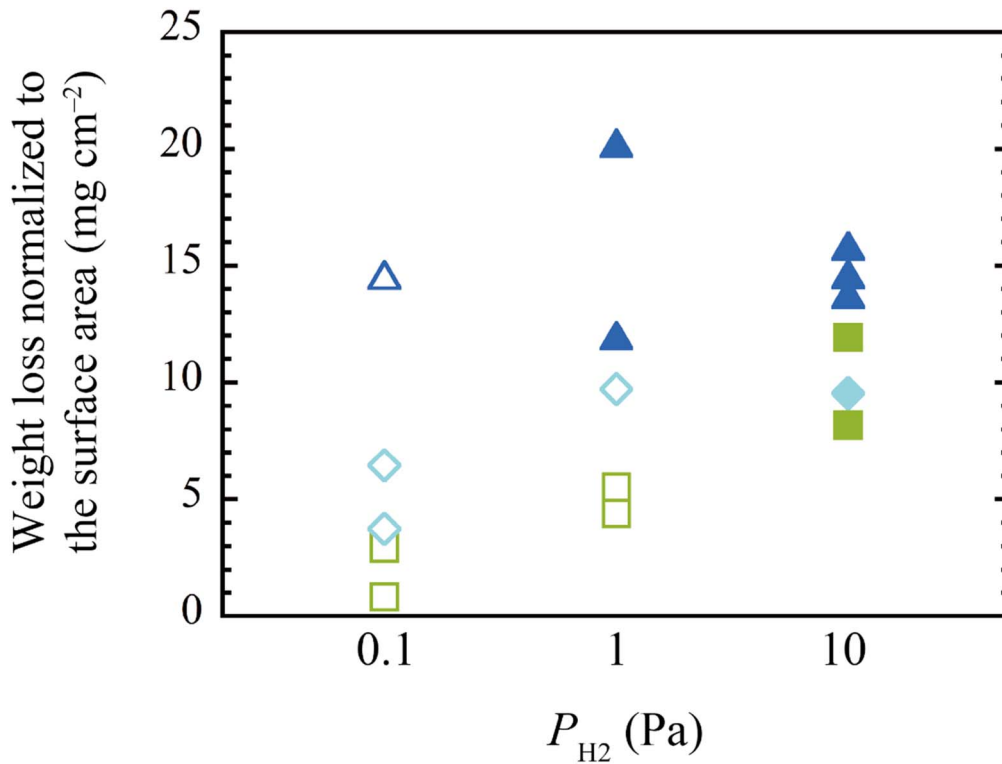


**Figure 3.** Histograms of the compositions of melilite crystallized under different conditions.  $P_{\text{H}_2} = 0.1$  Pa at the cooling rates of (a)  $50^\circ\text{C hr}^{-1}$  and (b)  $5^\circ\text{C hr}^{-1}$ .  $P_{\text{H}_2} = 1$  Pa at the cooling rates of (c)  $50^\circ\text{C hr}^{-1}$  and (d)  $5^\circ\text{C hr}^{-1}$ .  $P_{\text{H}_2} = 10$  Pa at the cooling rates of (e)  $50^\circ\text{C hr}^{-1}$  and (f)  $5^\circ\text{C hr}^{-1}$ . White (gray) bars are the melilite compositions of samples without (with) melilite mantle.

rates studied and at  $P_{\text{H}_2} = 1$  Pa with a slower cooling rate ( $5^\circ\text{C hr}^{-1}$ ). These melilites started to crystallize at the maximum temperature at  $P_{\text{H}_2} = 10$  Pa and during cooling at  $P_{\text{H}_2} = 1$  Pa (Table 1). The compositional zoning of melilite at the rim (Figure 2(b)) clearly shows that melilite crystallization proceeded from the sample surface toward the inside. The  $\text{\AA}k$ -poor melilite (less than  $\text{\AA}k_{21}$ ) is not expected to crystallize from the melt with the initial  $\text{CAI}_\chi$  composition based on equilibrium crystallization experiments in air (Table 1). This suggests that such  $\text{\AA}k$ -poor melilite crystallization observed in the samples with melilite mantle (Figures 3(d)–(f)) can be attributed to the depletion of Mg and Si near the melt surface, which was caused by evaporation of Mg and Si from the melt. This explains why, in the samples heated at  $P_{\text{H}_2} = 10$  Pa,

melilite crystallization occurred even at  $20^\circ\text{C}$  above the melilite crystallization temperature for the  $\text{CAI}_\chi$  composition.

The depletion of Mg and Si near the melt surface requires that the evaporation of Mg and Si dominates the elemental diffusion within the melt and prevents chemical homogenization (Richter et al. 2002; Mendybaev et al. 2006). The evaporation rates of Mg and Si from the melt in a hydrogen-dominant environment are proportional to the square root of  $P_{\text{H}_2}$  (Richter et al. 2002; Mendybaev et al. 2006), whereas the diffusion rate does not depend on  $P_{\text{H}_2}$ . At higher  $P_{\text{H}_2}$ , the effective evaporation of Mg and Si results in their depletion at the rim, leading to the crystallization of Al-rich melilite from the surface. However, at lower  $P_{\text{H}_2}$ , elemental diffusion dominates over evaporation. In this case, no chemical zoning



**Figure 4.** Weight losses of the samples heated at  $P_{\text{H}_2} = 0.1, 1,$  and  $10$  Pa. The samples cooled at  $50, 20, 5^\circ\text{C hr}^{-1}$  are represented by light green square, light blue diamond, dark blue triangles, respectively. Open (filled) symbols represent the samples without (with) complete melilite mantle.

in the melt is expected, and melilite crystallization should take place randomly in the chemically homogeneous melt. This should result in the crystallization of melilite in a narrower range of composition than in the former case (Figure 3).

The formation of the melilite mantle could suppress further evaporation from the melt. At  $P_{\text{H}_2} = 10$  Pa, the evaporative weight losses of the melt increased by only a factor of two with an increase in the cooling timescale by one order of magnitude (Figure 4). Moreover, crystallized melilite had a similar chemical compositional range, irrespective of the cooling rate (Figures 3(e), (f)). These observations are consistent with the closed system crystallization of most melilite crystals in the melt interior after the development of the melilite mantle.

However, evaporation of Mg and Si from the melt is not prevented when the melilite mantle does not form. Thus, evaporative weight loss should reflect the difference in evaporation rates. The larger weight loss at  $P_{\text{H}_2} = 1$  Pa and a cooling rate of  $50^\circ\text{C hr}^{-1}$  than at  $P_{\text{H}_2} = 0.1$  Pa (Figure 4) can be explained by the enhanced evaporation rate at  $P_{\text{H}_2} = 1$  Pa. The greater degree of evaporation at  $P_{\text{H}_2} = 1$  Pa led to the crystallization of more Åk-poor melilite than at  $P_{\text{H}_2} = 0.1$  Pa (Figures 3(a), (c)).

#### 4.2. Formation Conditions of Type B CAIs Indicated from Petrological and Chemical Characteristics

The experiments conducted in this study showed that both type B1 and B2 CAI-like textures can be reproduced under protosolar disk-like hydrogen pressure conditions; the former is formed at relatively high  $P_{\text{H}_2}$  and the latter at low  $P_{\text{H}_2}$ , as suggested by Mendybaev et al. (2006). The  $P_{\text{H}_2}$  required for the formation of type B1-like melilite mantle was 10 Pa, and that for type B2-like texture was 0.1 Pa (Table 1). At the intermediate  $P_{\text{H}_2}$  of 1 Pa, type B1-like structure formed when

the cooling rate was  $5^\circ\text{C hr}^{-1}$ , whereas type B2-like structure required the cooling rate faster than  $20^\circ\text{C hr}^{-1}$ . This boundary  $P_{\text{H}_2}$  condition of  $P_{\text{H}_2} = 1$  Pa is consistent with that predicted by Mendybaev et al. (2006).

The increase in åkermanite content from the CAI rim to the interior as shown in Figure 2(b) is also observed in natural type B1 CAIs (e.g., MacPherson & Grossman 1981; Simon & Grossman 2006; Kawasaki et al. 2018). Simon & Grossman (2006) showed that melilite in type B1 CAIs has a wider compositional range ( $\text{Åk}_{\sim 5-80}$ ) than that in type B2 CAIs, which is consistent with the experimental results at  $P_{\text{H}_2} = 10$  Pa (Figure 3). Melilite in type B2 CAIs is systematically more åkermanitic (Mg-rich) than that in type B1 CAIs, which is also consistent with the observations in the present study (Figure 3). Simon & Grossman (2006) argued that the presence/absence of melilite mantle in type B1 and B2 CAIs is likely due to the difference in their bulk chemical compositions. However, the present experiments clearly indicate that textural and compositional differences in type B1 and B2 melilite can be reproduced by crystallization of the precursor melt with the same bulk chemical composition in an open system under different  $P_{\text{H}_2}$  conditions.

#### 4.3. Implication for the Astrophysical Setting of Type B CAI Formation

The present study suggests that the CAI formation required (1) local fluctuation of the disk gas pressure ( $\geq 1$  Pa for type B1 and  $\leq 1$  Pa for type B2 CAIs), (2) regional variation of disk gas pressure, or (3) different cooling rates at  $P_{\text{H}_2} \sim 1$  Pa.

Fluctuation of the inner edge of the protoplanetary disk has been suggested to explain oxygen isotope variation within minerals in type B CAIs (Itoh & Yurimoto 2003; Yurimoto et al. 2008; Kawasaki et al. 2018). In this case, the fluctuation of disk edge would also cause the local fluctuation of disk gas pressure.

If CAIs are formed in the high-temperature region of protoplanetary disks (e.g., Yang & Ciesla 2012; Pignatale et al. 2018), the regional variation of disk gas pressure was expected because of radial dependence of disk surface density. Movement of CAI precursors along the vertical density structure of the disk (Aléon 2016) could also be responsible for the pressure variation discussed here.

A variation of cooling rates at  $P_{\text{H}_2} \sim 1$  Pa would also put a constraint on the mechanism of transient heating process for CAI melting.


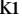
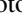
In any case, a hydrogen pressure of  $\sim 1$  Pa with some fluctuation was needed for the formation of type B CAIs. The hydrogen pressure conditions during the formation of type B CAIs ( $\geq 1$  Pa for type B1 and  $\leq 1$  Pa for type B2 CAIs), estimated from experiments under the protosolar disk-like low-pressure hydrogen in this study, would impose quantitative constraints on the astrophysical settings of the earliest epoch of the solar system evolution.

## 5. Conclusions

The hydrogen pressure during type B CAI formation in the early solar system was constrained through crystallization experiments of a type B CAI analog melt in an open system under low  $P_{\text{H}_2}$  conditions. The present experiments suggest that evaporation during partial melting events of type B CAIs plays an important role in determining the chemical, mineralogical, and petrologic characteristics of igneous CAIs. In particular, the melilite mantle of type B1 CAIs formed due to the depletion of Mg and Si near the surface of the melt, caused by enhanced evaporation at  $P_{\text{H}_2}$  larger than  $\sim 1$  Pa. This suggests that a  $P_{\text{H}_2}$  greater than  $\sim 1$  Pa is required for the formation of type B1 CAIs in the protosolar disk.

The authors appreciate the careful reviews and constructive comments of two anonymous reviewers. We thank T. Nagai for permitting us to use the one-atmosphere vertical furnace to synthesize the CAI analog and conduct the crystallization experiments in air. We are also grateful to the Astromaterials Science Research Group (JAXA) for kindly allowing us to use SEM-EDS. This work is financially supported by a Grant-in-Aid for JSPS Research Fellow (20J11855) and the Ministry of Education, Sports, Science, and Technology KAKENHI grants.

## ORCID iDs

Shogo Tachibana  <https://orcid.org/0000-0002-4603-9440>  
 Daiki Yamamoto  <https://orcid.org/0000-0001-6852-2954>  
 Noriyuki Kawasaki  <https://orcid.org/0000-0001-6502-6488>  
 Hisayoshi Yurimoto  <https://orcid.org/0000-0003-7072-0533>

## References

- Aléon, J. 2016, *E&PSL*, **440**, 62  
 Amelin, Y., Kaltenbach, A., Iizuka, T., et al. 2010, *E&PSL*, **300**, 343  
 Bullock, E. S., Knight, K. B., Richter, F. M., et al. 2013, *M&PS*, **48**, 1440  
 Clayton, R. N., Hinton, R. W., & Davis, A. M. 1988, *RSPTA*, **325**, 483  
 Connelly, J. N., Bizzarro, M., Krot, A. N., et al. 2012, *Sci*, **338**, 651  
 Davis, A. M., Hashimoto, A., Clayton, R. N., & Mayeda, T. K. 1990, *Natur*, **347**, 655  
 Grossman, L. 1972, *GeCoA*, **36**, 597  
 Grossman, L. 2010, *M&PS*, **45**, 7  
 Grossman, L., Ebel, D. S., Simon, S. B., et al. 2000, *GeCoA*, **64**, 2879  
 Grossman, L., Ebel, D. S., & Simon, S. B. 2002, *GeCoA*, **66**, 145  
 Itoh, S., & Yurimoto, H. 2003, *Natur*, **423**, 728  
 Kawasaki, N., Park, C., Sakamoto, N., et al. 2019, *E&PSL*, **511**, 25  
 Kawasaki, N., Simon, S. B., Grossman, L., et al. 2018, *GeCoA*, **221**, 318  
 Lange, R. A., & Carmichael, I. S. 1987, *GeCoA*, **51**, 2931  
 MacPherson, G. J., & Grossman, L. 1981, *E&PSL*, **52**, 16  
 Mendybaev, R. A., Kamibayashi, M., Teng, F. Z., et al. 2021, *GeCoA*, **292**, 557  
 Mendybaev, R. A., Richter, F. M., & Davis, A. M. 2006, *GeCoA*, **70**, 2622  
 Nagahara, H., & Ozawa, K. 1996, *GeCoA*, **60**, 1445  
 Pignatale, F. C., Charnoz, S., Chaussidon, M., & Jacquet, E. 2018, *ApJL*, **867**, L23  
 Podosek, F. A., Zinner, E. K., Macpherson, G. J., et al. 1991, *GeCoA*, **55**, 1083  
 Richter, F. M., Davis, A. M., Ebel, D. S., & Hashimoto, A. 2002, *GeCoA*, **66**, 521  
 Richter, F. M., Janney, P. E., Mendybaev, R. A., et al. 2007, *GeCoA*, **71**, 5544  
 Shahar, A., & Young, E. D. 2007, *E&PSL*, **257**, 497  
 Simon, S. B., & Grossman, L. 2006, *GeCoA*, **70**, 780  
 Stolper, E. 1982, *GeCoA*, **46**, 2159  
 Stolper, E., & Paque, J. M. 1986, *GeCoA*, **50**, 1785  
 Tachibana, S., & Tsuchiyama, A. 1998, *GeCoA*, **62**, 2005  
 Tachibana, S., Tsuchiyama, A., & Nagahara, H. 2002, *GeCoA*, **66**, 713  
 Takigawa, A., Tachibana, S., Nagahara, H., et al. 2009, *ApJL*, **707**, L97  
 Tsuchiyama, A., Takahashi, T., & Tachibana, S. 1998, *MinJ*, **20**, 113  
 Wark, D. A., & Lovering, J. F. 1982, *GeCoA*, **46**, 2581  
 Yamamoto, D., Kawasaki, N., Tachibana, S., et al. 2021, *GeCoA*, **314**, 108  
 Yang, L., & Ciesla, F. J. 2012, *M&PS*, **47**, 99  
 Yurimoto, H., Krot, A. N., Choi, B., et al. 2008, in *Oxygen in the Solar System*, ed. G. J. MacPherson (Washington, DC: Mineralogical Society of America), 141